Multigrating design for integrated single-atom trapping, manipulation, and readout

Aiping Liu,[1,3] Jiawei Liu,[1,3] Wei Peng,[1,3] Xin-Biao Xu,[2,4] Guang-Jie Chen,[2,4] Xifeng Ren,[2,4] Qin Wang,[1,3,*] and Chang-Ling Zou[2,4,5,†]

[1]*Institute of Quantum Information and Technology, Nanjing University of Posts and Telecommunications, Nanjing 210003, China*
[2]*CAS Key Laboratory of Quantum Information, University of Science and Technology of China, Hefei 230026, China*
[3]*Broadband Wireless Communication and Sensor Network Technology, Key Laboratory of Ministry of Education, Nanjing University of Posts and Telecommunications, Nanjing 210003, China*
[4]*CAS Center for Excellence in Quantum Information and Quantum Physics, University of Science and Technology of China, Hefei 230026, China*
[5]*State Key Laboratory of Quantum Optics and Quantum Optics Devices, and Institute of Opto-Electronics, Shanxi University, Taiyuan 030006, China*

(Received 25 January 2022; accepted 12 May 2022; published 25 May 2022)

An on-chip multigrating device is proposed to interface single atoms and integrated photonic circuits, by guiding and focusing lasers to the area ∼10 μm above the chip for trapping, state manipulation, and readout of single rubidium atoms. For the optical dipole trap, two 850-nm laser beams are diffracted and overlapped to form the lattice of a single-atom dipole trap, with the diameter of the optical dipole trap being around 2.7 μm. Similar gratings are designed for guiding a 780-nm probe laser to excite and also collect the fluorescence of ^{87}Rb atoms. Such a device provides a compact solution for future applications of single atoms, including the single-photon source, single-atom quantum register, and single-atom quantum sensor.

DOI: 10.1103/PhysRevA.105.053520

I. INTRODUCTION

In the past decades, quantum information processing has been developed greatly by utilizing the quantum properties of atoms and photons, where both atom internal states and photonic states can provide the carrier for encoding, storing, and transporting quantum information [1–3]. A lot of effort has been dedicated to quantum information processing based on cold atoms [4–6] and photons [7,8]. Recently, photonic integrated chips have been widely applied in quantum information science and show great potential in extending the photonic quantum information processors to tens of qubits [9–12]. In contrast, most previous investigations of cold atoms are implemented with a conventional optical setup, which is cumbersome, sensitive to environment perturbations, and costly. Therefore the atomic chip has attracted tremendous attention in the past decades and has become one of the most important platforms to integrate the devices of cold-atom traps and atomic state manipulation on a single chip [13–18]. A similar goal is also pursued by the trapped-ion system, and the cointegration of the trapped chip and the photonic chip was demonstrated recently [19–22].

However, it is still challenging to integrate cold-atom devices and photonic devices on a single chip. For trapping an ensemble of atoms, various methods that are compatible with the photonic chip have been proposed, such as the microwire atomic potential trap [23], grating magneto-optical trap [24–28], and static-magnetic trap [29]. In these platforms, the state manipulation and readout of the cold-atom ensemble are still performed using free-space laser beam excitation and fluorescence collection. Although the enhanced photon-atom interactions have been extensively studied with photonic microstructures and single atoms recently [30–37], it is still unclear how to capture individual atoms on the photonic chip without free-space optical components. Therefore one important challenge now is how to interface integrated photonic devices with neutral atoms tens of micrometers above the chip, and eventually to incorporate the single-atom trap, state manipulation, and readout with on-chip photonic devices. Recently, waveguide-integrated diffraction grating has been demonstrated for delivering the free-space optical cooling beams for a magneto-optic trap, which provides a potential platform for the interface between the chip and the free-space atoms [38].

In this paper, the platform of a multigrating chip is designed for the trapping, manipulation, and readout of a single atom. The grating transforms and focuses the integrated waveguide mode on the free-space light beam, thus providing an efficient approach to interface the atoms and on-chip light. By designing four gratings arranged symmetrically, single atoms could be trapped in the optical dipole trap by two 850-nm laser beams that diffracted from two gratings, and the atoms could be excited and their emissions (780 nm) could be collected by the other two gratings. Our numerical simulation shows that the chip-to-free-space conversion has an efficiency of ∼45%, and the laser beam has a focus width of only ∼2.7 μm. As a result, with only 10 mW laser power in each waveguide, an optical dipole trap depth up to 0.85 mK

*qinw@njupt.edu.cn
†clzou321@ustc.edu.cn

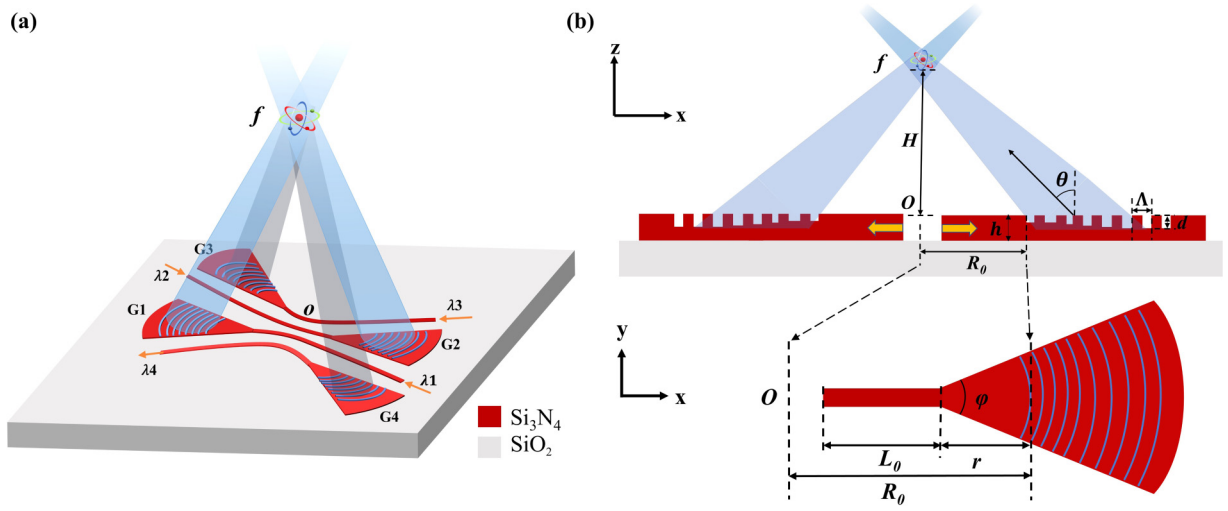

FIG. 1. (a) Schematic diagram of the multi-focusing-grating structure for a hybrid photonic-atom chip. (b) Detailed illustration of the grating from the side view (upper panel) and the top view (lower panel).

for the ^{87}Rb atom could be achieved. For the atomic state detection, 0.66% of the atomic fluorescence emission could be collected into the waveguide. Our proposal provides an experimentally feasible approach to incorporate single atoms and a photonic integrated chip, which holds great potential for future integrated atom or molecule arrays [6,39] and promise for hybrid quantum optics devices [40,41].

II. STRUCTURE AND PRINCIPLE

The proposed multigrating is based on a 300-nm-thick Si_3N_4 wafer with SiO_2 as the substrate. As shown in Fig. 1(a), the designed multigrating microstructure is composed of four fan-shaped focusing gratings denoted by G1, G2, G3, and G4, respectively, with a common symmetric center denoted by o. The gratings of G1 and G2 have a rotation of 65° relative to the gratings of G3 and G4. Due to the symmetry, it is expected that an atom at the center could be coupled with all gratings simultaneously. On one hand, the lasers guided in the waveguide could be diffracted to the free space by the gratings. As a reversal process, the photons emitted by the atom could be collected by the gratings and guided into the waveguide. In this paper, we apply this hybrid photonic-atomic chip design for ^{87}Rb: Gratings G1 and G2 are used to diffract 850-nm laser beams to form an optical dipole potential well for trapping the ^{87}Rb atom, and gratings G3 and G4 are used for guiding a 780-nm laser to excite and read out the fluorescence of the ^{87}Rb atom. It is worth noting that the design could be extended to other atomic species by varying the geometric parameters according to the working wavelengths.

For an efficient interface between the atom and the guided photon on the chip, the conversion between the free-space beam and the waveguide mode in the waveguide is most crucial. Figure 1(b) shows the detailed geometry of the grating, by which the light propagating in the grating could be diffracted and focused. The diffraction properties of the grating are mainly determined by three parameters: period Λ, etching depth d, and duty cycle η (the ratio of the unetched part to the entire cycle) [42]. According to the first-order Bragg condition, the period Λ of the grating is given by

$$\Lambda = \frac{\lambda}{n_{\text{eff}} - n_a \sin\theta}, \tag{1}$$

where λ is the wavelength of light in free space, n_{eff} is the effective refractive index of the guiding mode in the grating, θ is the diffraction angle, and n_a is the refractive index of the cladding above the grating with $n_a = 1$ for air. In order to obtain a focused Gaussian-like beam, all of the diffracted light from each groove of the grating is designed to be directed to the same point f. Then the diffraction angle θ_N of the Nth groove meets the condition

$$\tan\theta_N = -\frac{R_{N-1}}{H}, \tag{2}$$

where $R_{N-1} = R_0 + \Lambda_1 + \Lambda_2 + \Lambda_3 + \cdots + \Lambda_{N-1}$ is the location of the Nth groove, R_0 is the distance between the symmetric center o and the first groove of the grating, and H is the height of point f [Fig. 1(b)]. According to Eqs. (1) and (2), the period Λ varies along the grating to obtain the focused beam.

Besides, the curvature of the grating arcs should also be optimized for the focusing at f. The parabolic grating arc ($x \sim -y^2/2R$) is designed to ensure that each grating arc is parallel to the phase front of the wave incident on it. The intensity of the propagating light in the waveguide decreases along the grating due to the diffraction loss by the grating. An increased etching depth is designed along the grating to enhance the diffraction efficiency and thus compensate the propagating loss in the grating, since the diffraction efficiency increases with the etching depth.

III. RESULTS

To validate our designs, we performed three-dimensional finite-difference time-domain (FDTD) simulations to numerically analyze the optical field distribution on the grating. In the simulation, the transverse electric (TE) mode is adopted to be diffracted by the grating [43]. We choose the width of the

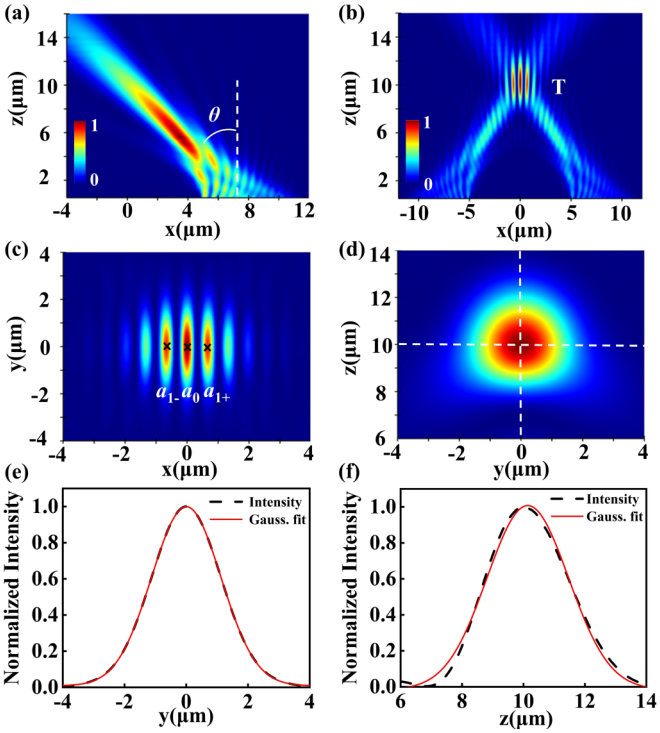

FIG. 2. The diffraction beams from the gratings. (a) The intensity distribution of the diffraction beam from a single grating in the x-z plane. (b)–(d) The intensity distribution of the interference field formed by the diffraction beams from two gratings in the x-z plane (b), (c) in the x-y plane, and (d) in the y-z plane. The positions of trapped centers are denoted by crosses in the antinodes a_{1-}, a_0, and a_{1+}. The same color bar is used for (b)–(d). (e) and (f) The intensity distributions along the y and z directions [along dashed lines in (d)], respectively.

waveguide to be 550 nm and the length and taper angle of the tapered waveguide to be $r = 2$ μm and $\varphi = 50°$, respectively. The length of the grating part is 8 μm with 18 grooves. The etching depth increases from 20 to 280 nm linearly, which can improve the diffraction efficiency of the grating [44]. Around the working wavelengths of 780 and 850 nm, the refractive index of Si_3N_4 and SiO_2 is set as 1.9935 and 1.45, respectively. For simplicity, the duty cycle η is set as 0.5.

A. Single-atom trapping

Figure 2(a) gives the intensity distribution of the diffraction beam from a single grating, which is designed for a focusing beam targeting at a working point height $H = 10$ μm with $R_0 = 4.5$ μm. From the intensity distribution in the x-z plane with $y = 0$, the diffracted beam has a diffraction angle θ of about $-36.87°$. As expected, the diffracted beam forms a focusing Gaussian-like beam with small divergence angle, with a waveguide-to-beam conversion efficiency of about 45.2%. The diffraction beam is focused on the point ($x = 3.5$ μm, $y = 0$, $z = 5.6$ μm) with a waist diameter of around 1.23 μm. It should be noted that the focus of the diffraction beam is deviated from the target working point ($x = 0$, $y = 0$, $z = 10$ μm), because there are practical limitations in designing the grating structures with a single grating arc

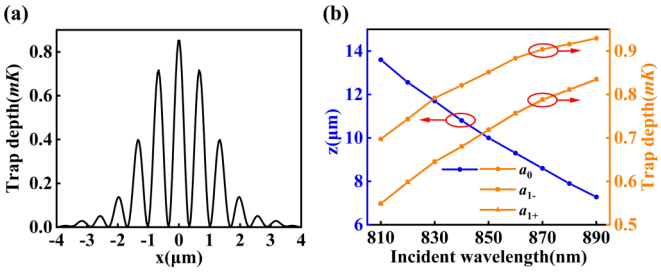

FIG. 3. The distribution of the optical dipole potential. (a) The trap depth of the optical dipole potential along the x direction. (b) The relation between the optical dipole trap and the incident wavelength.

shape. In this paper, the focus point of the parabolic grating arc ($x \sim -y^2/2R$) is ($x = R/2$, $y = 0$, $z = 0$), which point is on the top of the grating and could not be accessed by other gratings. Therefore we are employing two identical gratings, G1 and G2, that are designed and arranged symmetrically with their diffraction beam incident on the same point f to form a one-dimensional optical lattice at the target working point f at the center. It is also guaranteed that the atoms around f could be accessed by other gratings with similar design.

As shown in Fig. 2(b), two diffraction beams have the same diffraction angle of $-36.87°$ and overlap with each other to form a lattice of optical dipole traps for trapping ^{87}Rb atoms, with the antinodes (points of maximum laser intensities) located above the center $x = 0$ at a height of about 10 μm. The detailed intensity distribution in the x-y planes with $z = 10$ μm is shown in Fig. 2(c), where the interference of the two beams induces a fringe period of 0.67 μm along the x direction. In the plane perpendicular to the lattice direction, the optical field shows a Gaussian-like beam profile [Fig. 2(d)], indicating the confinement of atoms in the well in both y and z directions. In Figs. 2(e) and 2(f), the intensity distributions of the dipole laser field along the y and z directions are fitted by Gaussian functions, showing a very good agreement. The corresponding diameters of the Gaussian intensity distributions in Figs. 2(e) and 2(f) are 2.48 and 2.66 μm, respectively. For an input power of the 850-nm laser of 10 mW, the antinodes a_{1-}, a_0, and a_{1+} [as labeled in Fig. 2(c) at $x = -0.67$, 0, and 0.67 μm] have electric field intensities $|E|^2$ of 9.3×10^7, 1.1×10^8, and 9.3×10^7 $(\mathrm{V/cm})^2$, respectively.

For such a dipole trap lattice, by ignoring the Zeeman sublevels, the optical dipole potential could be estimated as [45]

$$U = \frac{\hbar \gamma I_0}{24 I_S}\left(\frac{1}{\delta_{1/2}} + \frac{2}{\delta_{3/2}}\right), \tag{3}$$

where $\gamma/2\pi \approx 6.1$ MHz is the natural linewidth in ^{87}Rb, I_S is the saturation intensity, $\delta_{1/2}$ and $\delta_{3/2}$ are the detunings between the laser frequency and the D1 and D2 transitions, respectively, and I_0 is the intensity of the optical field. For the ^{87}Rb atom with resonant wavelength at 780 nm, the gradient force formed by an optical field of 850 nm (red detuned with respect to both D1 and D2 transitions) is a conservative force, so the ^{87}Rb atoms could be trapped in the antinode.

Figure 3 gives the optical dipole trap depth formed by the interference field with a 10-mW laser incident on each of the gratings. The trap depth of the optical dipole well along

the line ($y = 0, z = 10\ \mu$m) for the 850-nm laser is shown in Fig. 3(a), where there are several optical dipole trap centers along the x direction. The trap depths formed by the optical dipole potential in antinodes a_{1-}, a_0, and a_{1+} are 0.72, 0.85, and 0.72 mK, respectively. By placing these beams into a standard magneto-optical trap (MOT), where the ^{87}Rb atoms are cooled to 100 μK, single atoms can be trapped successfully by the optical dipole well formed in these antinodes. According to previous experimental studies of single-atom trapping in tweezers [46], our gratings provide dipole traps with a beam waist that is smaller than 3 μm, thus satisfying the criteria for the atomic collision blockade [45] in the trap, and we could expect at most one atom in each antinode. Since the platform is based on the transparent and optically flat photonic membrane of SiO_2, the laser cooling and optical control of cold atoms can be formed above the transparent membrane [33]. The platform of multigrating is practical to trap single atoms in experiments.

Since the trap field is formed by the diffraction of gratings, the optical dipole potential is related to the incident laser wavelength. In Fig. 3(b), the relation between the optical dipole potential and the dipole laser wavelength is numerically investigated. When the wavelength varies from 810 to 890 nm, the angle and the diffraction efficiency of the beam change. We found that the optical dipole trap of antinode a_0 (a_{1-} or a_{1+}) increases from 0.70 (0.55) mK to 0.93 (0.84) mK and the height of the antinode a_0 changes from 13.6 to 7.28 μm. Due to the structural symmetry, the positions of the antinodes are unchanged in the x and y directions. Since the optical properties of the microstructures are determined by the dimensionless parameters Λ/λ or R_N/λ, the robustness of the grating against the wavelength difference also indicates the robustness of our device against the geometric parameter uncertainty due to fabrication imperfections. Therefore our multigrating design provides a feasible optical dipole trap with a broad bandwidth for practical experiments.

B. Single-atom transport

Since the integrated photonic chip holds promise for high-performance thermal-optic [47] or electro-optic modulators [48], we would like to transport the atoms in the dipole traps. As the interference of two diffraction beams is related to the incident phase, the intensity distribution of the optical field can be manipulated by precisely controlling the laser phases. Figure 4 gives the intensity distributions on the x-y plane with $z = 10\ \mu$m with different incident phase difference $\Delta\varphi = \varphi_1 - \varphi_2$, where φ_1 and φ_2 are the incident phases of G1 and G2, respectively. By increasing the incident phase difference $\Delta\varphi$, the antinodes move right, and their intensities are changed as shown in Figs. 4(a1)–4(e1) with incident phase difference $\Delta\varphi = 0^\circ$, 90°, 180°, 270°, and 360°, respectively. When the incident phase difference $\Delta\varphi$ changes from 0° to 180°, the antinodes are changed to nodes, and the nodes are changed to antinodes. The interference pattern on the x-z plane with $y = 0$ has similar properties to that on the x-y plane with $z = 10\ \mu$m as shown in Figs. 4(a2)–4(e2). The lines in Fig. 4(f) give the relations between the offsets of the antinodes and the incident phase difference $\Delta\varphi$. When the incident phase difference increases from 0° to 360°, the

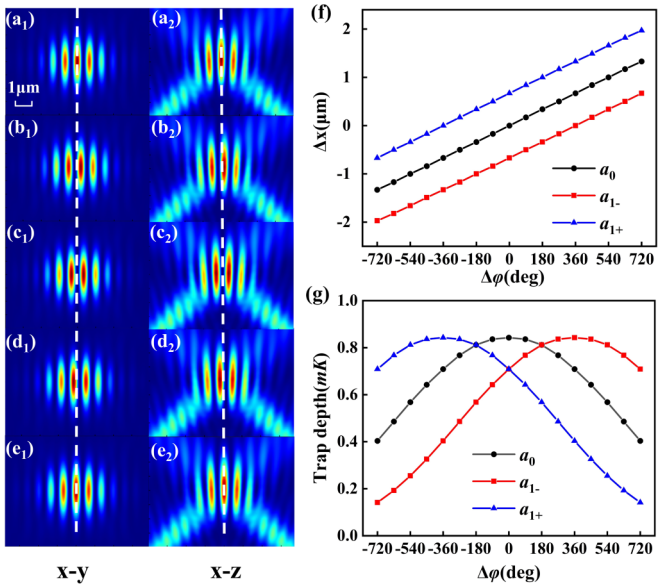

FIG. 4. The intensity distributions of the interference beams with different incident phase differences, (a1)–(e1) on the x-y plane and (a2)–(e2) on the x-z plane, with incident phase differences of 0°, 90°, 180°, 270°, and 360°, respectively. The offsets of antinodes (f) and the optical dipole potentials (g) vary with the incident phase differences.

antinodes move right linearly with a period of 0.67 μm. That is, the antinode a_{1-} moves to the position of former antinode a_0, and the antinode a_0 moves to the position of former antinode a_{1+}. The optical dipole traps formed by the antinodes also change with the incident phase difference $\Delta\varphi$ as shown by the curves in Fig. 4(g). The trap depths of the optical dipole potential decrease with the positions of antinodes far away from the center, which is related to the incident phase difference $\Delta\varphi$.

Benefiting from the fact that the optical dipole trap of the antinode can be manipulated by the incident phase difference, the platform of multigrating can be used to trap single atoms. There is more than one antinode, such as antinodes a_{1-}, a_0, and a_{1+}, that can trap atoms. According to the collision blockade, the loading rate of an atom in a single dipole trap is around 50% [49]; thus utilizing the lattice has the potential to enhance the loading rate. When there are multiple atoms loaded in the lattice, it is possible to only keep a single atom at the center a_0. By tuning the phase of the incident laser, the unwanted atoms could be released from the lattice as the depth of the optical dipole potential wells decreases when moving away from the center. After that, only the antinode a_0 contains the trapped atoms.

C. State manipulation and readout

For an integrated photonic-atom chip, both the trapping and manipulation of the atom are necessary and important for information processing. Besides gratings G1 and G2, which are used to trap the cold ^{87}Rb atoms using 850-nm laser beams, similar gratings—gratings G3 and G4—are designed for 780-nm light to excite and read out the fluorescence of the ^{87}Rb atoms. Similar to the design for the dipole trap

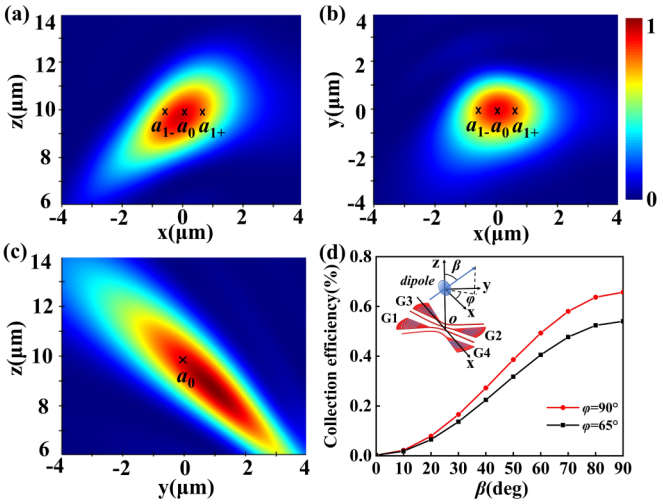

FIG. 5. The intensity distributions of the optical field diffracted from grating G3 incident with the 780-nm laser on the (a) x-z plane, (b) x-y plane, and (c) y-z plane. (d) The collection efficiency of grating G3 varies with the angle of dipole polarization for 780 nm.

laser, G3 and G4 could be optimized with slightly different parameters. Similarly, G3 and G4 are arranged symmetrically to the center o, which has a rotation of 65° relative to gratings G1 and G2 as shown in Fig. 1(a). Figures 5(a) and 5(b) give the intensity distributions of the optical field on the x-z and x-y planes diffracted from grating G3, respectively. The diffraction efficiency of grating G3 is about 47.6%. In this multigrating platform, the trapped ^{87}Rb atoms can be excited by the diffraction of light from grating G3, and the same for grating G4. With an incident laser power in the waveguide as low as 1 μW at 780 nm, the electric field strength $|E|$ on trap centers a_{1-}, a_0, and a_{1+} is 6.7×10^3, 7.7×10^3, and 7.1×10^3 (V/m), corresponding to a coherent Rabi frequency of $\Omega/2\pi = 360$, 416, and 384 MHz, respectively. Therefore, in our configuration, the atoms could be efficiently manipulated with very low power consumption.

As a reversal process of excitation, the grating could also be utilized for collecting the atom emission. Since the waveguide mode is converted to a Gaussian beam in free space, the grating is equivalent to a lens with a numerical aperture (NA) of around 0.5, while the waveguide-to-beam conversion introduces an insertion loss due to the imperfect diffraction to other directions and also to the substrates. Therefore we also expect a considerable atom fluorescence collection efficiency from single atoms with comparing with a conventional composite lens. For instance, in a typical experimental setup with a NA = 0.5 [50], the collection efficiency is about 2%, and by accounting for the attenuation due to the polarization selection and the reflection of the grating, the efficiency of the fluorescence collection is estimated to be around 0.3%.

For a concrete estimation of the collection efficiency of the single-photon emissions from the atom, we numerically solved the energy flux in the waveguide by placing a dipole at o. The results for the collection efficiency of grating G3 at 780 nm, which varies with the angle β between the dipole polarization and the z axis, are summarized in Fig. 5(d). The red and black curves correspond to the dipole polarization with $\varphi = 90°$ and 65°, respectively. When the dipole polarization is parallel to the grating groove, that is, $\beta = 90°$ and $\varphi = 90°$, an approximate collection efficiency of 0.66% is obtained. Considering the spontaneous emission with random polarization, the total collection efficiency is about 0.22%, which agrees with the above estimations. With a high collection efficiency, the designed multigrating is feasible to use for fluorescence collection, and there is the potential to realize entanglement between atoms on the same chip through photonic Bell state measurement [51].

IV. CONCLUSION

In summary, a hybrid photonic-atomic integrated platform based on multigrating is proposed for on-chip atom trapping, atomic state manipulation, and readout. For the optical dipole trap, two 10-mW 850-nm laser light beams are diffracted by two gratings to form an optical dipole trap of up to 0.85 mK for a ^{87}Rb atom. The atoms could be confined in an optical dipole trap with a potential well radius of around 1.4 μm, efficiently excited by the microwatt-level on-chip 780-nm laser power, and collected with an efficiency of 0.66%. The design could be extended to other atom species and could also be extended to even more gratings. For instance, a two-dimensional atom lattice could be realized by dipole-trap lasers from three or four gratings. Further optimization of the grating structure is possible by more sophisticated chip-to-free-space conversion devices, such as metasurfaces [52]. Our device is compatible with other on-chip photonic devices, and it is possible to integrate all essential optical devices for controlling and manipulating atoms on a single chip. Therefore our work provides a unique approach to realize scalable atom arrays, which hold great potential for applications in sensing, metrology [53,54], and quantum information processing [4,6,55].

ACKNOWLEDGMENTS

This work was supported by a project funded by the China Postdoctoral Science Foundation (SBH190004), National Key Research and Development Program of China (2018YFA0306400 and 2017YFA0304100), and Leading-Edge Technology Program of Jiangsu Natural Science Foundation (BK20192001). X.-B.X., X.R., Q.W., and C.-L.Z. are supported by the National Natural Science Foundation of China (Grants No. 11922411, No. 62061160487, No. 12074194, No. 12104441, and No. U21A6006), the Natural Science Foundation of Anhui Province (Grant No. 2108085MA22), and the Fundamental Research Funds for the Central Universities. The numerical calculations in this paper have been done on the supercomputing system in the Supercomputing Center of University of Science and Technology of China.

[1] C. Monroe, Quantum information processing with atoms and photons, Nature (London) **416**, 238 (2002).

[2] C. Weedbrook, S. Pirandola, R. García-Patrón, N. J. Cerf, T. C. Ralph, J. H. Shapiro, and S. Lloyd, Gaussian

quantum information, Rev. Mod. Phys. **84**, 621 (2012).
[3] S. Wehner, D. Elkouss, and R. Hanson, Quantum internet: A vision for the road ahead, Science **362**, eaam9288 (2018).
[4] M. Saffman, T. G. Walker, and K. Mølmer, Quantum information with Rydberg atoms, Rev. Mod. Phys. **82**, 2313 (2010).
[5] F. Schäfer, T. Fukuhara, S. Sugawa, Y. Takasu, and Y. Takahashi, Tools for quantum simulation with ultracold atoms in optical lattices, Nat. Rev. Phys. **2**, 411 (2020).
[6] A. M. Kaufman and K.-K. Ni, Quantum science with optical tweezer arrays of ultracold atoms and molecules, Nat. Phys. **17**, 1324 (2021).
[7] M. V. Larsen, X. Guo, C. R. Breum, J. S. Neergaard-Nielsen, and U. L. Andersen, Deterministic generation of a two-dimensional cluster state, Science **366**, 369 (2019).
[8] H.-S. Zhong, H. Wang, Y.-H. Deng, M.-C. Chen, L.-C. Peng, Y.-H. Luo, J. Qin, D. Wu, X. Ding, Y. Hu, X.-Y. Yang, W.-J. Zhang, H. Li, Y. Li, X. Jiang, L. Gan, G. Yang, L. You, Z. Wang, L. Li *et al.*, Quantum computational advantage using photons, Science **370**, 1460 (2020).
[9] A. Liu, M. Wu, R. Zhuang, J. Hong, Q. Wang, and X. Ren, On-chip generation of the reconfigurable orbital angular momentum with high order, Opt. Express **28**, 17957 (2020).
[10] W. Bogaerts, D. Pérez, J. Capmany, D. A. Miller, J. Poon, D. Englund, F. Morichetti, and A. Melloni, Programmable photonic circuits, Nature (London) **586**, 207 (2020).
[11] J. Wang, F. Sciarrino, A. Laing, and M. G. Thompson, Integrated photonic quantum technologies, Nat. Photonics **14**, 273 (2020).
[12] T. K. Paraïso, T. Roger, D. G. Marangon, I. De Marco, M. Sanzaro, R. I. Woodward, J. F. Dynes, Z. Yuan, and A. J. Shields, A photonic integrated quantum secure communication system, Nat. Photonics **15**, 850 (2021).
[13] W. Hänsel, P. Hommelhoff, T. Hänsch, and J. Reichel, Bose–Einstein condensation on a microelectronic chip, Nature (London) **413**, 498 (2001).
[14] T. Schumm, S. Hofferberth, L. M. Andersson, S. Wildermuth, S. Groth, I. Bar-Joseph, J. Schmiedmayer, and P. Krüger, Matter-wave interferometry in a double well on an atom chip, Nat. Phys. **1**, 57 (2005).
[15] P. Böhi, M. F. Riedel, J. Hoffrogge, J. Reichel, T. W. Hänsch, and P. Treutlein, Coherent manipulation of Bose–Einstein condensates with state-dependent microwave potentials on an atom chip, Nat. Phys. **5**, 592 (2009).
[16] M. F. Riedel, P. Böhi, Y. Li, T. W. Hänsch, A. Sinatra, and P. Treutlein, Atom-chip-based generation of entanglement for quantum metrology, Nature (London) **464**, 1170 (2010).
[17] S. Machluf, Y. Japha, and R. Folman, Coherent Stern–Gerlach momentum splitting on an atom chip, Nat. Commun. **4**, 2424 (2013).
[18] H. Hattermann, D. Bothner, L. Ley, B. Ferdinand, D. Wiedmaier, L. Sárkány, R. Kleiner, D. Koelle, and J. Fortágh, Coupling ultracold atoms to a superconducting coplanar waveguide resonator, Nat. Commun. **8**, 2254 (2017).
[19] K. K. Mehta, C. D. Bruzewicz, R. McConnell, R. J. Ram, J. M. Sage, and J. Chiaverini, Integrated optical addressing of an ion qubit, Nat. Nanotechnol. **11**, 1066 (2016).
[20] K. K. Mehta, C. Zhang, M. Malinowski, T.-L. Nguyen, M. Stadler, and J. P. Home, Integrated optical multi-ion quantum logic, Nature (London) **586**, 533 (2020).
[21] R. J. Niffenegger, J. Stuart, C. Sorace-Agaskar, D. Kharas, S. Bramhavar, C. D. Bruzewicz, W. Loh, R. T. Maxson, R. McConnell, D. Reens, G. N. West, J. M. Sage, and J. Chiaverini, Integrated multi-wavelength control of an ion qubit, Nature (London) **586**, 538 (2020).
[22] Z. D. Romaszko, S. Hong, M. Siegele, R. K. Puddy, F. R. Lebrun-Gallagher, S. Weidt, and W. K. Hensinger, Engineering of microfabricated ion traps and integration of advanced on-chip features, Nat. Rev. Phys. **2**, 285 (2020).
[23] J. Schmiedmayer, Guiding and trapping a neutral atom on a wire, Phys. Rev. A **52**, R13 (1995).
[24] C. Nshii, M. Vangeleyn, J. P. Cotter, P. F. Griffin, E. Hinds, C. N. Ironside, P. See, A. Sinclair, E. Riis, and A. S. Arnold, A surface-patterned chip as a strong source of ultracold atoms for quantum technologies, Nat. Nanotechnol. **8**, 321 (2013).
[25] J. Cotter, J. McGilligan, P. Griffin, I. Rabey, K. Docherty, E. Riis, A. Arnold, and E. Hinds, Design and fabrication of diffractive atom chips for laser cooling and trapping, Appl. Phys. B: Lasers Opt. **122**, 172 (2016).
[26] J. P. McGilligan, P. F. Griffin, E. Riis, and A. S. Arnold, Diffraction-grating characterization for cold-atom experiments, J. Opt. Soc. Am. B **33**, 1271 (2016).
[27] J. P. Mcgilligan, K. Moore, A. Dellis, G. Martinez, E. de Clercq, P. Griffin, A. Arnold, E. Riis, R. Boudot, and J. Kitching, Laser cooling in a chip-scale platform, Appl. Phys. Lett. **117**, 054001 (2020).
[28] L. Chen, C.-J. Huang, X.-B. Xu, Y.-C. Zhang, D.-Q. Ma, Z.-T. Lu, Z.-B. Wang, G.-J. Chen, J.-Z. Zhang, H. X. Tang, C.-H. Dong, W. Liu, G.-Y. Xiang, G.-C. Guo, and C.-L. Zou, Planar-Integrated Magneto-Optical Trap, Phys. Rev. Applied **17**, 034031 (2022).
[29] J. Reichel, W. Hänsel, and T. W. Hänsch, Atomic Micromanipulation with Magnetic Surface Traps, Phys. Rev. Lett. **83**, 3398 (1999).
[30] M. Kohnen, M. Succo, P. G. Petrov, R. A. Nyman, M. Trupke, and E. A. Hinds, An array of integrated atom–photon junctions, Nat. Photonics **5**, 35 (2011).
[31] C. Stehle, H. Bender, C. Zimmermann, D. Kern, M. Fleischer, and S. Slama, Plasmonically tailored micropotentials for ultracold atoms, Nat. Photonics **5**, 494 (2011).
[32] A. Goban, C.-L. Hung, S.-P. Yu, J. Hood, J. Muniz, J. Lee, M. Martin, A. McClung, K. Choi, D. Chang, O. Painter, and H. Kimble, Atom–light interactions in photonic crystals, Nat. Commun. **5**, 3808 (2014).
[33] M. E. Kim, T.-H. Chang, B. M. Fields, C.-A. Chen, and C.-L. Hung, Trapping single atoms on a nanophotonic circuit with configurable tweezer lattices, Nat. Commun. **10**, 1647 (2019).
[34] K. P. Nayak, J. Wang, and J. Keloth, Real-Time Observation of Single Atoms Trapped and Interfaced to a Nanofiber Cavity, Phys. Rev. Lett. **123**, 213602 (2019).
[35] J.-B. Béguin, A. P. Burgers, X. Luan, Z. Qin, S. P. Yu, and H. J. Kimble, Advanced apparatus for the integration of nanophotonics and cold atoms, Optica **7**, 1 (2020).
[36] X. Luan, J.-B. Béguin, A. P. Burgers, Z. Qin, S.-P. Yu, and H. J. Kimble, The integration of photonic crystal waveguides with atom arrays in optical tweezers, Adv. Quantum Technol. **3**, 2000008 (2020).
[37] T. Đorđević, P. Samutpraphoot, P. L. Ocola, H. Bernien, B. Grinkemeyer, I. Dimitrova, V. Vuletić, and M. D. Lukin,

Entanglement transport and a nanophotonic interface for atoms in optical tweezers, Science **373**, 1511 (2021).

[38] N. Chauhan, D. Bose, M. Puckett, R. Moreira, K. Nelson, and D. J. Blumenthal, Photonic integrated Si_3N_4 ultra-large-area grating waveguide MOT interface for 3D atomic clock laser cooling, in *2019 Conference on Lasers and Electro-Optics (CLEO)* (IEEE, Piscataway, NJ, 2019), pp. 1–2.

[39] L. Anderegg, L. W. Cheuk, Y. Bao, S. Burchesky, W. Ketterle, K.-K. Ni, and J. M. Doyle, An optical tweezer array of ultracold molecules, Science **365**, 1156 (2019).

[40] A. W. Elshaari, W. Pernice, K. Srinivasan, O. Benson, and V. Zwiller, Hybrid integrated quantum photonic circuits, Nat. Photonics **14**, 285 (2020).

[41] E. Pelucchi, G. Fagas, I. Aharonovich, D. Englund, E. Figueroa, Q. Gong, H. Hannes, J. Liu, C.-Y. Lu, N. Matsuda, J.-W. Pan, F. Schreck, F. Sciarrino, C. Silberhorn, J. Wang, and K. D. Jöns, The potential and global outlook of integrated photonics for quantum technologies, Nat. Rev. Phys. **4**, 194 (2022).

[42] D. Taillaert, P. Bienstman, and R. Baets, Compact efficient broadband grating coupler for silicon-on-insulator waveguides, Opt. Lett. **29**, 2749 (2004).

[43] J. C. C. Mak, Q. Wilmart, S. Olivier, S. Menezo, and J. K. S. Poon, Silicon nitride-on-silicon bi-layer grating couplers designed by a global optimization method, Opt. Express **26**, 13656 (2018).

[44] L. Wu, K. Qiu, and S. Fu, Fine-tuning the etch depth profile via dynamic shielding of ion beam, Nucl. Instrum. Methods Phys. Res., Sect. B **381**, 72 (2016).

[45] K. L. Corwin, S. J. M. Kuppens, D. Cho, and C. E. Wieman, Spin-Polarized Atoms in a Circularly Polarized Optical Dipole Trap, Phys. Rev. Lett. **83**, 1311 (1999).

[46] D. Frese, B. Ueberholz, S. Kuhr, W. Alt, D. Schrader, V. Gomer, and D. Meschede, Single Atoms in an Optical Dipole Trap: Towards a Deterministic Source of Cold Atoms, Phys. Rev. Lett. **85**, 3777 (2000).

[47] S. Idres and H. Hashemi, Low-power SiN thermo-optic phase modulator operating in red visible wavelength range, in *2020 Conference on Lasers and Electro-Optics (CLEO)* (OSA, Washington, DC, 2020), p. JTh2B.7.

[48] G. Liang, H. Huang, A. Mohanty, M. C. Shin, X. Ji, M. J. Carter, S. Shrestha, M. Lipson, and N. Yu, Robust, efficient, micrometre-scale phase modulators at visible wavelengths, Nat. Photonics **15**, 908 (2021).

[49] N. Schlosser, G. Reymond, and P. Grangier, Collisional Blockade in Microscopic Optical Dipole Traps, Phys. Rev. Lett. **89**, 023005 (2002).

[50] R. Garthoff, Efficient single photon collection for single atom quantum nodes, Ph.D. thesis, Ludwig Maximilian University, 2021.

[51] T. van Leent, M. Bock, F. Fertig, R. Garthoff, S. Eppelt, Y. Zhou, P. Malik, M. Seubert, T. Bauer, W. Rosenfeld, W. Zhang, C. Becher, and H. Weinfurter, Entangling single atoms over 33 km telecom fibre, arXiv:2111.15526.

[52] K. Huang, Z. Dong, S. Mei, L. Zhang, Y. Liu, H. Liu, H. Zhu, J. Teng, B. Luk'yanchuk, J. K. Yang, and C.-W. Qiu, Silicon multi-meta-holograms for the broadband visible light, Laser Photonics Rev. **10**, 500 (2016).

[53] M. A. Norcia, A. W. Young, W. J. Eckner, E. Oelker, J. Ye, and A. M. Kaufman, Seconds-scale coherence on an optical clock transition in a tweezer array, Science **366**, 93 (2019).

[54] A. W. Young, W. J. Eckner, W. R. Milner, D. Kedar, M. A. Norcia, E. Oelker, N. Schine, J. Ye, and A. M. Kaufman, Half-minute-scale atomic coherence and high relative stability in a tweezer clock, Nature (London) **588**, 408 (2020).

[55] M. Saffman, Quantum computing with neutral atoms, Nat. Sci. Rev. **6**, 24 (2019).